# Waveform modeling and inversion of ambient noise cross-correlation functions in a coastal ocean environment

Xiaoqin Zang, Michael G. Brown, and Oleg A. Godin

---

## ARTICLES YOU MAY BE INTERESTED IN

Extracting coherent wave fronts from acoustic ambient noise in the ocean
The Journal of the Acoustical Society of America **116**, 1995 (2004); https://doi.org/10.1121/1.1797754

Acoustic noise interferometry in a time-dependent coastal ocean
The Journal of the Acoustical Society of America **143**, 595 (2018); https://doi.org/10.1121/1.5022287

Head waves in ocean acoustic ambient noise: Measurements and modeling
The Journal of the Acoustical Society of America **143**, 1182 (2018); https://doi.org/10.1121/1.5024332

Compressive geoacoustic inversion using ambient noise
The Journal of the Acoustical Society of America **135**, 1245 (2014); https://doi.org/10.1121/1.4864792

Cross-correlation function of acoustic fields generated by random high-frequency sources
The Journal of the Acoustical Society of America **128**, 600 (2010); https://doi.org/10.1121/1.3458815

Variability of the coherent arrivals extracted from low-frequency deep-ocean ambient noise correlations
The Journal of the Acoustical Society of America **138**, 521 (2015); https://doi.org/10.1121/1.4923447

---

# Waveform modeling and inversion of ambient noise cross-correlation functions in a coastal ocean environment

Xiaoqin Zang[a)] and Michael G. Brown
*Rosenstiel School of Marine and Atmospheric Science, University of Miami, 4600 Rickenbacker Causeway, Miami, Florida 33149, USA*

Oleg A. Godin[b)]
*Cooperative Institute for Research in Environmental Sciences, University of Colorado Mail Code R/PSD, 325 Broadway, Boulder, Colorado 80305, USA*

Theoretical studies have shown that cross-correlation functions (CFs) of time series of ambient noise measured at two locations yield approximations to the Green's functions (GFs) that describe propagation between those locations. Specifically, CFs are estimates of weighted GFs. In this paper, it is demonstrated that measured CFs in the 20–70 Hz band can be accurately modeled as weighted GFs using ambient noise data collected in the Florida Straits at ∼100 m depth with horizontal separations of 5 and 10 km. Two weighting functions are employed. These account for (1) the dipole radiation pattern produced by a near-surface source, and (2) coherence loss of surface-reflecting energy in time-averaged CFs resulting from tidal fluctuations. After describing the relationship between CFs and GFs, the inverse problem is considered and is shown to result in an environmental model for which agreement between computed and simulated CFs is good.
© 2015 Acoustical Society of America. [http://dx.doi.org/10.1121/1.4928303]

## I. INTRODUCTION

The process by which approximations to Green's functions (GFs) between two locations are estimated by cross-correlating time series of ambient noise recorded at those two locations is widely referred to as noise interferometry (NI). The underlying theory is now well developed.[1–13] NI has proven to be extremely useful in remote sensing applications, including seismic applications,[14–17] helioseismic applications,[18,19] atmospheric acoustic applications,[20–22] structural health monitoring,[23,24] and ocean infragravity wave studies.[25] The utility of NI in underwater acoustic applications,[26–34] including passive echosounder applications,[35–37] has also been demonstrated. In underwater acoustic applications of NI, most investigators have focused on extracting estimates of the travel times of temporally resolved multipaths from measured CFs. But, in situations in which multipaths are not temporally resolved, the extraction of information from a measured CF suitable for use in an inverse analysis requires that one carefully considers and accounts for subtle differences between CFs and GFs. That is the case in the data that is analyzed here. Also, it should be noted that, even when multipath arrivals are temporally resolved in measured CFs, the accuracy of travel time estimates can be significantly improved if CF waveform (phase) information is exploited.[38] Thus, from a remote sensing perspective, there is strong motivation to carefully examine the relationship between CFs and GFs. Using data collected in the Straits of Florida, that relationship is explored here. Both the forward problem of simulating CFs, and the inverse problem of finding the environmental model that gives the best-fitting CF are considered here.

The data set analyzed here was collected in December 2012 in an NI experiment conducted in the Straits of Florida. Figure 1 shows the location of the three ambient noise recording systems that were deployed, and the water column sound speed structure measured at the beginning of the six-day time window that was used to produce the measured CFs used in this paper. Those CFs, for instrument pairs 1-2 and 2-3, are shown in Fig. 2. Preliminary experimental results and some details relating to signal processing are described by Brown *et al.*[39] Close examination of the CFs for both the 1-2 and 2-3 instrument pairs reveals a small, but measurable, current-induced timing shift of the energetic portion of the CFs at both positive and negative lag. That topic, including estimation of the current from the measured CFs, is discussed in Godin *et al.*[40] For the analysis presented in this paper, the current-induced timing shifts at both positive and negative lag have been removed, and the resulting positive and negative lag portions of the CFs have been summed. This is done both to slightly improve the signal-to-noise ratio (SNR) of the CFs that we analyze here, and to insure consistency with the assumption made here of a stationary environment.

Section II focuses on the relationship between CFs and GFs, and the forward problem of numerically simulating CFs. It is argued that, for the data set considered here, CFs must be modeled as weighted and phase-shifted GFs. The two dominant weighting functions for the data set considered are introduced and discussed. Section III considers the
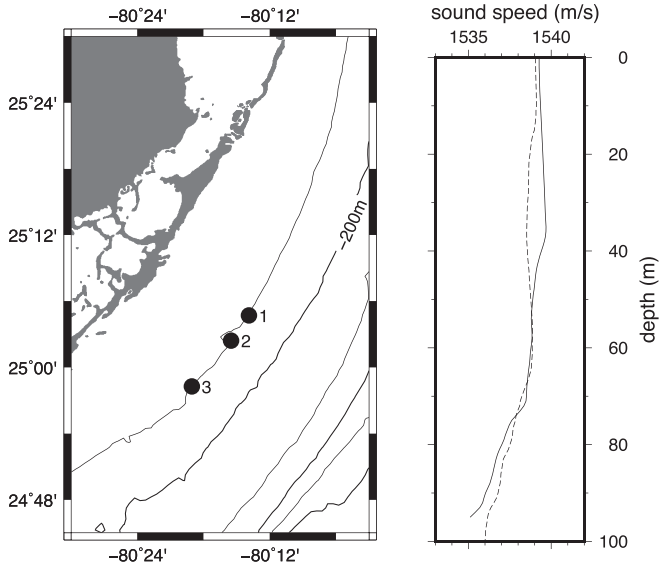
FIG. 1. (Left) Map showing the locations of instruments 1, 2, and 3 in the December 2012 Florida Straits NI experiment. The depth contour interval is 100 m. (Right) Sound speed profiles measured in the vicinity of instruments 1 (dashed curve) and 3 (solid curve).

inverse problem of finding the environmental model for which a suitable measure of misfit between measured and simulated CFs is minimized. That exercise may be thought of as a simple extension of the ideas presented in Sec. II. Our results are discussed in Sec. IV and summarized in Sec. V.

## II. CF WAVEFORM MODELING: THE FORWARD PROBLEM

The basic mathematical result underlying acoustic NI is that the cross-correlation function (CF), $C_{AB}(t)$, of time series of acoustic pressure ambient noise at locations $\mathbf{x}_A$ and $\mathbf{x}_B$ satisfies

$$\frac{d}{dt}C_{AB}(t) = D(t) * [G(\mathbf{x}_B|\mathbf{x}_A, -t) - G(\mathbf{x}_A|\mathbf{x}_B, t)]. \quad (1)$$

where $D(t)$ is an approximation to a delta function, "$*$" denotes convolution, and the transient GF $G(\mathbf{x}|\mathbf{x}_0, t)$ satisfies

$$\left(\nabla^2 - \frac{1}{c^2(\mathbf{x})}\frac{\partial^2}{\partial t^2}\right)G(\mathbf{x}|\mathbf{x}_0, t) = -\frac{\delta(r)}{2\pi r}\delta(z - z_0)\delta(t),$$
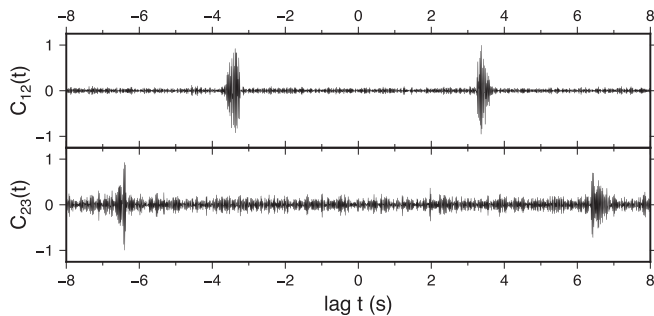
$$(2)$$



FIG. 2. Six-day coherent averages of CFs corresponding to instrument pairs 1-2 (top), and 2-3 (bottom) measured during the December 2012 NI experiment.

where $\mathbf{x} = (x, y, z)$, $\mathbf{x}_0 = (0, 0, z_0)$, and $r = (x^2 + y^2)^{1/2}$. Because Eq. (1) plays a critical role in the results presented below, a self-contained derivation of that equation is included as an Appendix to this paper. The GFs are causal; the positive (negative) lag portion of $C_{AB}(t)$ describes propagation from $\mathbf{x}_B$ to $\mathbf{x}_A$ ($\mathbf{x}_A$ to $\mathbf{x}_B$). Consistent with Eq. (2), we assume here that the environment is stationary, so $G(\mathbf{x}_B|\mathbf{x}_A, t) = G(\mathbf{x}_A|\mathbf{x}_B, t)$ by reciprocity. With this assumption, it follows from Eq. (1) that the negative lag structure of $C_{AB}(t)$ is redundant and that for $t > 0$,

$$\frac{d}{dt}C_{AB}(t) = -D(t) * G(\mathbf{x}_A|\mathbf{x}_B, t). \quad (3)$$

The normal mode representation of $\bar{G}(\mathbf{x}_A|\mathbf{x}_B, \omega)$, the Fourier transform of $G(\mathbf{x}_A|\mathbf{x}_B, t)$, is well known.[42] (Note that unlike Eq. (3), the normal mode representation assumes a layered medium.) Consistent with Eq. (3), the normal mode representation of $\bar{C}_{AB}(\omega)$, satisfies $-i\omega\bar{C}_{AB}(\omega) = -\bar{D}(\omega)\bar{G}(\mathbf{x}_A|\mathbf{x}_B, \omega)$, or

$$\bar{C}_{AB}(\omega) = \bar{D}(\omega)\left(\frac{1}{i\omega}\right)\left(\frac{i}{4}\right)\sum_m \psi_m(z_A)$$

$$\times \psi_m(z_B)H_0^{(1)}(k_m(\omega)r_{AB}), \quad (4)$$

where the normal modes, which are defined on the depth interval $(-\infty, 0]$ are assumed to be normalized, $\int_{-\infty}^0 \psi_m^2(z)\,dz = 1$, and $r_{AB}$ is the horizontal separation between $\mathbf{x}_A$ and $\mathbf{x}_B$.

A straightforward derivation of Eq. (1) (see the Appendix) involves making use of an exact identity involving GFs, Eq. (A9), together with the highly idealized assumption, Eq. (A1), that noise sources are delta-correlated in space and time. The latter assumption is clearly an approximation. In spite of this, Eq. (1) and, hence, also Eqs. (3) and (4) remain useful approximate results provided the distribution of noise sources is approximately diffuse. To account for physical processes that are not accounted for in the derivation of Eq. (1), including a diffuse but nonuniform distribution of noise sources, a weighting function[26] can be included on the right-hand side of Eq. (4).

The weighting function used here is a product of two terms. The first accounts for the fact that in the frequency band used here to construct CFs, 20–70 Hz, noise sources, including shipping and wind-related noise, are predominantly near-surface sources.[41] (Seismic sources also contribute to ambient noise in this frequency band, but there was no known nearby exploration geophysics activity during our experiment, or experimental evidence of its presence.) The pressure-release boundary condition at the air–sea interface then leads to a dipole radiation pattern, with $\sin\theta$ weighting, where $\theta$ is the propagation angle at the sea surface measured relative to the horizontal. The relevance of the dipole excitation weighting in underwater acoustic NI applications was first pointed out by Roux et al.[26] The second term in the weighting function that we employ accounts for the fact that tidal fluctuations lead to phase fluctuations—and thus coherence loss—of surface reflecting energy, which is partially filtered out by the phase-coherent processing that we perform.

Note in this regard that the CFs analyzed here were produced by coherently stacking short-time CF estimates over a duration (~6 days) that is long compared to the M2 tidal period, and that energy at higher frequency and steeper propagation angles is most susceptible to tidal-fluctuation-induced coherence loss. To quantify the effect of tidal fluctuations, consider a homogeneous ocean with sound speed $c$ and constant depth $h$, subject to a tidal perturbation $\delta h$. Let $r_{hc}$ denote the range of a half ray cycle of a surface- and bottom-reflecting ray connecting fixed instruments. At range $r$, the number of half ray cycles is $r/r_{hc} = r \tan \theta / h$. For each half ray cycle, the path length perturbation is $\delta h \sin \theta$. The total tidal-induced path length perturbation over range $r$ is then $(r \delta h / h) \sin \theta \tan \theta$ and the total phase perturbation is $\Delta \phi(\omega, \theta) = (\omega/c)(r \delta h / h) \sin \theta \tan \theta$. It is shown in Sec. 9.8 of Brekhovskikh and Lysanov[43] that if phase fluctuations have a Gaussian pdf, the mean coherent field is weighted by the function $\exp(-(\Delta \phi)^2 / 2)$ where $\Delta \phi$ is evaluated with $\delta h$ set equal to its root-mean-square value. In our simulations, this expression for the tidal-fluctuation-induced coherence loss weighting function was used with $\delta h$ set equal to 0.45 m, consistent with relevant environmental conditions.

With the above comments in mind, our simulated CFs are computed by evaluating a weighted form of Eq. (4),

$$\bar{C}_{AB}(\omega) = \bar{D}(\omega) \left( \frac{1}{4\omega} \right) \sum_m W(\omega, \theta_m) \psi_m(z_A)$$
$$\times \psi_m(z_B) H_0^{(1)}(k_m(\omega) r_{AB}), \tag{5}$$

where $W(\omega, \theta_m) = \sin \theta_m \exp(-(\Delta \phi(\omega, \theta_m))^2 / 2)$. Note that $\theta_m$ depends on both mode number and frequency, consistent with the modal quantization condition, and the relationship $k_m = (\omega/c) \cos \theta_m$. Consistent with the manner in which measured CFs were processed, $\bar{D}(\omega)$ was chosen to be a Hanning window with zeros at 20 and 70 Hz. Fourier transforming $\bar{C}_{AB}(\omega)$ back to the time domain gives $C_{AB}(t)$. All calculations shown below were performed using a slightly modified form of the KRAKEN[44] normal mode model.

## III. CF WAVEFORM MODELING: THE INVERSE PROBLEM

The results presented in Sec. II rely on approximate and possibly incomplete descriptions of relevant physical processes. The validity of our mathematical description of these processes needs to be demonstrated by showing equivalence between measured and simulated CFs. But such a comparison is complicated by environmental uncertainty. In this section, we describe a simple procedure to test our ability to reproduce, using Eq. (5), measured CF waveforms, while simultaneously allowing for plausible environmental uncertainty. The ocean sound speed structure and bathymetry were well characterized during the experiment. There is much greater uncertainty in the seafloor structure and, in the 20–70 Hz band of interest, the influence of the seafloor structure on the water column sound field is expected to be significant. Thus, our inverse analysis focuses on seafloor structure together with uncertainty [of O(10 m)] in the horizontal separation $r$ between instruments.

With these comments in mind, our inverse analysis focuses on $r$ and parameters that describe the seafloor structure, using some assumed parameterization. We focus on CFs estimated using the 1-2 instrument pair, corresponding to $r$ of ~5.01 km. We focus on the 1-2 instrument pair for two reasons: (1) the SNR for the 1-2 instrument pair is higher than that for the 2-3 instrument pair, and (2) the assumption of range-independent bathymetry is a much better approximation for the 1-2 pair than for the 2-3 pair. Note that the mathematical expression for the weighting function that was introduced in Sec. II was greatly simplified by the assumption that the environment is range independent.

The following simple procedure is used to investigate the inverse problem. A parameterization of the environment is chosen, together with suitable bounds on the model parameters. A brute-force search over the relevant parameter space is then conducted. For each combination of model parameters, a suitable measure of misfit between simulated and measured CFs is computed. The optimal set of model parameters is then chosen to be the set that minimizes the misfit. For the results shown, the misfit was defined as

$$M(\mathbf{p}) = \int_{t_{start}}^{t_{end}} [C_m(t) - C_s(\mathbf{p}, t)]^2 dt, \tag{6}$$

where the elements of the vector $\mathbf{p}$ are the model parameters, $C_m(t)$ is the measured CF, and $C_s(\mathbf{p}, t)$ is the simulated CF. Because there is no absolute amplitude scale for $C_m(t)$, both $C_m(t)$ and $C_s(\mathbf{p}, t)$ in Eq. (6) are normalized so that their maximum absolute amplitudes are equal to 1. For the 1-2 pair $t_{start}$ and $t_{end}$ were set equal to 3.2 s and 3.7 s, respectively. The procedure just described can be claimed to lead to an optimal solution for the range of parameter values explored, but it is important to keep in mind that inversion results depend on how one chooses to parameterize the environment. For that reason, no claim to uniqueness can be made. Several different environmental parameterizations have been explored. Two of these are discussed below. With guidance from a nearby seismic section[45] in a similar geological setting, both parameterizations considered here assume that the seafloor is a two-layer structure consisting of a sediment layer overlying a substrate. Parameter limits were chosen, in part, using guidance from Jensen et al.[46] and, in part, to insure that the minimum of the misfit function could fall on a parameter limit only if a physical argument prevented that limit from being exceeded.

First, consider an environmental model consisting of a fluid sediment layer overlying a rigid bottom. We shall refer to this as the four-parameter model. The four parameters that we seek to estimate are the sediment sound speed $c_s$, the sediment density $\rho_s$, the sediment layer thickness $d_s$, and the range $r$. A comparison of the measured CF and the best-fitting four-parameter simulated CF is shown in Fig. 3. Figure 4 shows two two-dimensional slices of the corresponding misfit function $M(c_s, d_s)$ for fixed $\rho_s$, $r$, and $M(\rho_s, r)$ for fixed $c_s, d_s$. Figure 4 also shows limits on the search domain of the four unknown parameters. Not surprisingly, the misfit $M$ is less sensitive to $\rho_s$ than the other three parameters. Minimizing the misfit function that we have
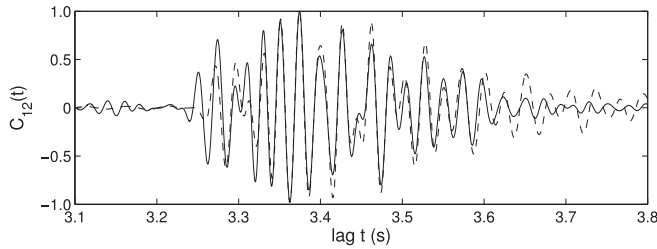
J. Acoust. Soc. Am. **138** (3), September 2015

Zang *et al.* 1327

FIG. 3. Measured CF (solid curve) and best-fitting four-parameter simulated CF (dashed curve) for the 1-2 instrument pair.



FIG. 5. Measured 1-2 instrument pair CF (solid curve) and corresponding simulated CF (dashed curve) computed using the optimal eight-parameter environmental model with $W = \sin\theta \exp(-(\Delta\phi)^2/2)$.

chosen, Eq. (6), imposes a high penalty for a phase mismatch, so it is not surprising that the phases of measured and simulated CFs in Fig. 3 are in generally better agreement than the amplitudes.

Next, we consider a slightly more general lossy fluid model with eight unknown parameters: the sediment layer sound speed $c_s$, the sediment layer thickness $d_s$, the sediment layer density $\rho_s$, the sediment layer attenuation $\alpha_s$, the substrate (bottom) sound speed $c_b$, the substrate density $\rho_b$, the substrate attenuation $\alpha_b$, and the range $r$. A comparison of the measured CF and the best-fitting eight-parameter simulated CF is shown in Fig. 5. Figure 6 shows two two-dimensional slices of the corresponding misfit function: $M(c_b, r)$ for fixed $c_s$, $d_s$, $\rho_s$, $\alpha_s$, $\rho_b$, and $\alpha_b$, and $M(d_s, c_s)$ for fixed $\rho_s$, $\alpha_s$, $c_b$, $\rho_b$, $\alpha_b$, and $r$. Figure 6 also shows the limits of the search domain for the unknown parameters $r$, $c_s$, $d_s$, and $c_b$. The other four parameter searches were bounded by the limits $1.2 < \rho_s/\rho_{\text{ocean}} < 1.7$, $1.7 < \rho_b/\rho_{\text{ocean}} < 3.0$, $0 < \alpha_s < 1.0$ dB/$\lambda$, and $0 < \alpha_b < 1.2$ dB/$\lambda$.

## IV. DISCUSSION

The results presented in Sec. III are representative of a much larger set of qualitatively similar results. Other environmental model parameterizations have been explored, as have other choices of the misfit function. As noted above, the type of analysis performed allows one to make only very qualified statements about optimality and uniqueness of the solution found; these issues are related to each other, and are

strongly tied to, and constrained by, the assumptions that one makes about how to parameterize the environment. Some specific comments about the results presented above follow.

Although the four-parameter model corresponding to the CF shown in Fig. 3 is optimal in the sense that we have described, that solution appears to have a significant defect: the leading edge of the energetic portion of the simulated CF appears to be one cycle out of phase with the measured CF. Consistent with this observation, the estimated value of $r$, 5.030 km, is a larger correction, 20 m, to the navigational estimate than we expect. Convergence to a poor solution is due to a combination of the choice of the misfit function (recall the comments in Sec. III about the misfit function imposing a high penalty on relative phase mismatch) and an overly restrictive parameterization of the environment. As a result, we have little confidence in the estimated four-parameter model solution. That model will not be further discussed.

In contrast, there is no obvious problem associated with the solution found using the eight-parameter model (see Fig. 5). The optimal parameters found using the eight-parameter model are $r = 5.000$ km, $c_s = 1570$ m/s, $d_s = 9.0$ m, $\rho_s/\rho_{\text{ocean}} = 1.30$, $\alpha_s = 0$, $c_b = 1800$ m/s, $\rho_b/\rho_{\text{ocean}} = 2.20$, and $\alpha_b = 0.8$ dB/$\lambda$. We have estimated domains of uncertainty for each of these parameters by varying each parameter independently, keeping the others fixed at their optimal values. Lower and upper bounds
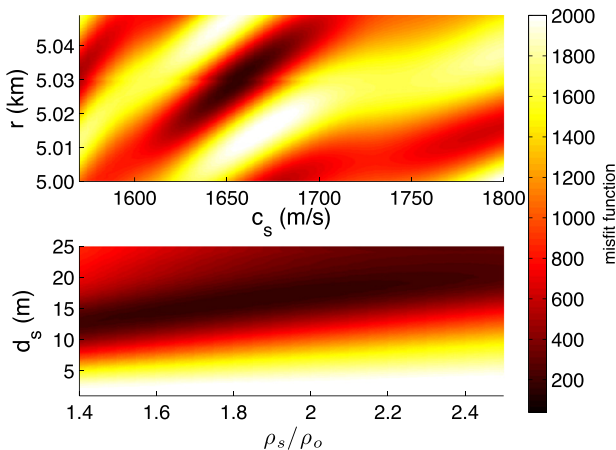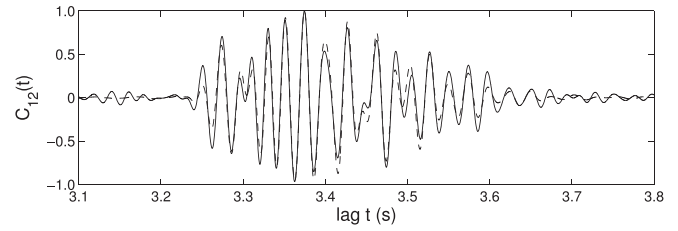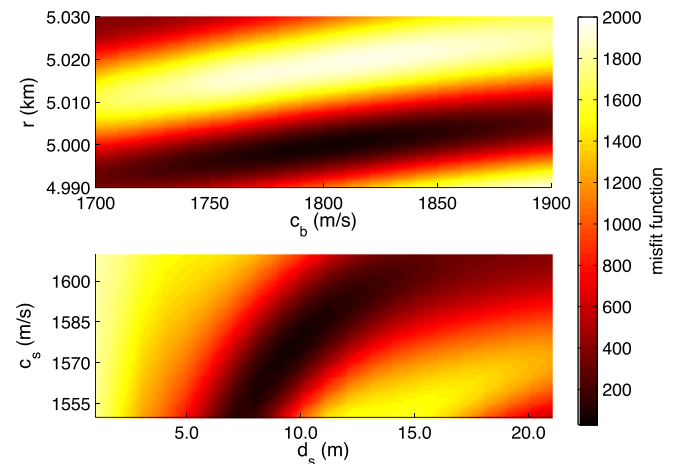


FIG. 4. (Color online) Two two-dimensional slices of the four-parameter misfit function for the 1-2 instrument pair: $M(c_s, d_s)$ for $\rho_s/\rho_{\text{ocean}} = 1.90$, $r = 5.030$ km; and $M(\rho_s/\rho_{\text{ocean}}, r)$ for $c_s = 1655$ m/s, $d_s = 17$ m.



FIG. 6. (Color online) Two two-dimensional slices of the eight-parameter misfit function for the 1-2 instrument pair: $M(c_b, r)$ for $c_s = 1570$ m/s, $d_s = 9$ m, $\rho_s/\rho_{\text{ocean}} = 1.3$, $\alpha_s = 0$, $\rho_b/\rho_{\text{ocean}} = 2.2$, $\alpha_b = 0.8$ dB/$\lambda$; and $M(d_s, c_s)$ for $r = 5.000$ km, $\rho_s/\rho_{\text{ocean}} = 1.3$, $\alpha_s = 0$, $c_b = 1800$ m/s, $\rho_b/\rho_{\text{ocean}} = 2.2$, $\alpha_b = 0.8$ dB/$\lambda$.

1328    J. Acoust. Soc. Am. **138** (3), September 2015

Zang *et al.*

on the uncertainty domain for the varied parameter were then estimated as the nearest parameter values for which the misfit $M$ is higher than the absolute minimum, $M_{min}$, of the misfit function by an amount equal to 1% of the total range of $M$ over the entire search domain. (Although the choice of the threshold value of $M$ is somewhat arbitrary, this exercise gives a good idea of the range of parameters for which agreement between measured and simulated CFs is very good.) The procedure just described gives the following bounds: $4.999\,km < r < 5.001\,km$, $1567\,m/s < c_s < 1575\,m/s$, $8.8\,m < d_s < 9.2\,m$, $1.24 < \rho_s/\rho_{ocean} < 1.36$, $0\,dB/\lambda < \alpha_s < 0.42\,dB/\lambda$, $1789\,m/s < c_b < 1814\,m/s$, $2.09 < \rho_b/\rho_{ocean} < 2.27$, and $0.2\,dB/\lambda < \alpha_b < 2.0\,dB/\lambda$. It is clear from these bounds that our inversion results do not provide strong constraints on estimates of $\alpha_s$ and $\alpha_b$. Consistent with the assumed structure of our eight-parameter model and our sediment layer thickness estimate, a seismic section at a site in a geologically similar setting ($\sim15\,km$ from the Florida Keys in water of $\sim100\,m$ deep and $\sim100\,km$ to the southwest of our experimental site) reveals a sediment layer, whose thickness is $\sim10\,m$, overlying a limestone formation.[45] It is difficult to provide a quantitative assessment of any of our other geo-acoustic parameter estimates. Jiang et al.[47] and Monjo et al.[48] also performed geo-acoustic inversions using data collected at sites that are approximately 120 and 230 km, respectively, north of our experimental site, but in deeper water where the sediment layer thickness is greater. Those authors and the references they cite (which list non-acoustic measurements of bottom properties in the Florida Straits) report a very broad range of parameter values, including values of parameters that we have not considered like porosity, shear wave speed and attenuation, and compressional speed gradients. Compressional wave speed estimates in the sediment range from 1540 m/s (Ref. 48) to 1683 m/s.[47]

Some features of the simulated CF based on the optimal eight-parameter environmental model will now be described. Figure 7 shows spectra of measured and simulated CFs. Agreement is seen to be good. Recall that a Hanning window has been applied to both spectra, so no insight into how well the inversion procedure worked can be gleaned by comparing spectral envelopes. In contrast, the locations of the zeros in the spectrum of the simulated CF have not been constrained in any way, so the good agreement between the
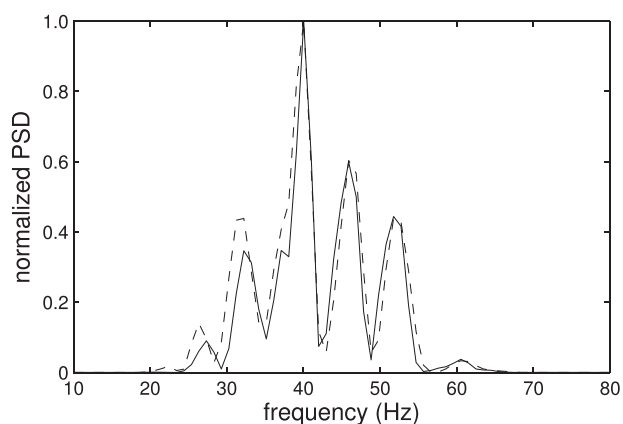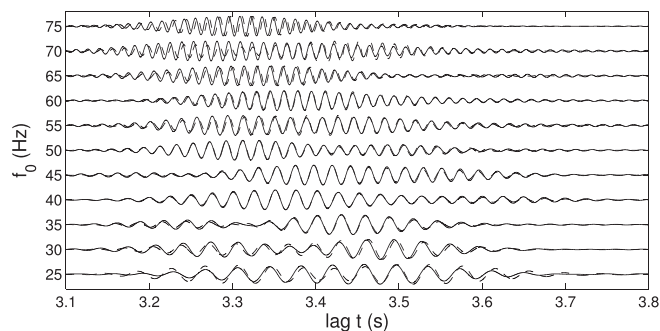


FIG. 8. Measured CF (solid curves) and best-fitting eight-parameter simulated CF (dashed curves) for the 1-2 instrument pair in overlapping 10 Hz bands.

locations of the zeros in the spectra of the simulated and measured CFs gives one confidence that the estimated environmental model is close to the true environment. Figure 8 shows measured and simulated CFs in overlapping narrow (10 Hz) frequency bands. Within each 10 Hz band a Hanning window weighting function was applied, and each band-limited CF was normalized individually. Agreement between measured and simulated CFs is seen to be good in all frequency bands shown. Again, this gives confidence that the estimated environmental model is close to the true environment.

We turn our attention now to analysis of the CF estimated using the 2-3 instrument pair. The estimated navigational separation between those instruments is 9.76 km. The low SNR of the CF for this instrument pair (see Figs. 2 and 9) poses an obvious limitation. Also, along the path between the 2-3 instrument pair the bottom depth varied between 86 and 100 m, compared to variations between 97 and 101 m along the path between the 1-2 instrument pair. To model propagation between the 2-3 instrument pair, the range-independent assumption is not realistic. The combination of low SNR and a range-dependent environment led us to give up on the idea of performing the same type of analysis of this data that was performed using the CFs estimated using the 1-2 instrument pair. Instead, we use this data set as a consistency test on the model parameters that were estimated using the 1-2 instrument pair inverse analysis described above. A comparison of measured and simulated CFs for the 2-3 instrument pair is shown in Fig. 9. To perform the simulation, an adiabatic mode calculation[44,46] was performed. Such a calculation is expected to be accurate because bathymetric variations were gradual. The adiabatic mode calculation was performed assuming the sediment layer thickness was constant and that all bottom parameters are identical to those described above, based on the 1-2 instrument pair analysis. Note, however, that while the environment is assumed fixed in this calculation, uncertainty in the range between instruments 2 and 3 must be allowed and accounted for. This led to a one-parameter inverse problem that was solved the same way the four- and eight-parameter inverse problems described in Sec. III were solved. The adiabatic mode calculation shown in Fig. 9 corresponds to the best-fitting value of $r$. The optimal value of $r$ was found to be 9.775 km, which deviates by 15 m from the nominal navigation-based



FIG. 7. Spectra of measured CF (solid curve) and best-fitting eight-parameter simulated CF (dashed curve) for the 1-2 instrument pair.
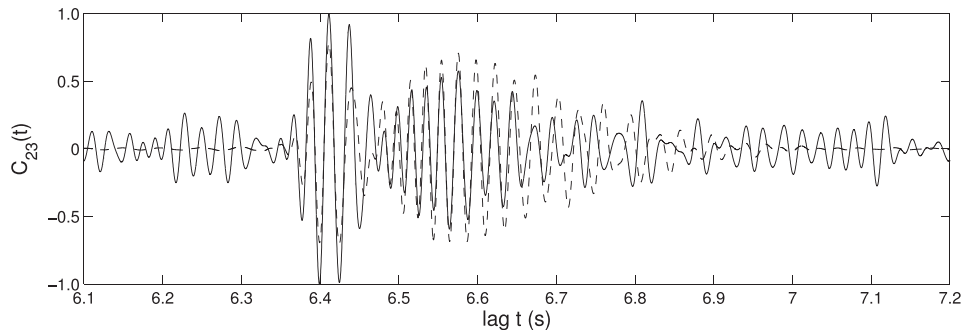
FIG. 9. Measured CF (solid curve) and simulated CF (dashed curve) for the 2-3 instrument pair.

estimate. Considering the relatively low SNR of the measured CF, agreement between measured and simulated CFs in Fig. 9 is fairly good. On the time interval from 6.35 s to 7.0 s the correlation coefficient between measured and simulated CFs is 70.6%.

We now address the question of whether inclusion of the weighting function $W(\omega, \theta_m)$ improves agreement between measured and simulated CFs. Figure 10 shows a comparison of the measured broadband (20–70 Hz) CF for the 1-2 instrument pair with an unweighted ($W = 1$) simulation, computed using the optimal parameter values listed above. Recall that Fig. 5 shows a comparison of the same measured CF with a weighted [using $W = \sin\theta\exp(-(\Delta\phi)^2/2)$] simulated CF. When comparing Figs. 5 and 10, it is useful to keep in mind that the early arriving energy—prior to $\sim$3.35 s—is low-angle energy that is strongly damped in Fig. 5 by the term $\sin\theta$; later-arriving energy is higher angle energy that is damped by both $\sin\theta$ and $\exp(-(\Delta\phi)^2/2)$, with neither term dominant. Also, all CFs plotted in both Figs. 5 and 10 are normalized to have maximum absolute amplitude equal to 1, which partially obscures the aforementioned damping. (Some normalization assumption must be made because there is no absolute amplitude scale for measured CFs.) Differences between Figs. 5 and 10 are small; with the aforementioned normalization, correlation coefficients between measured and simulated CFs are 96.3% when $W = \sin\theta\exp(-(\Delta\phi)^2/2)$ (Fig. 5) is used and 94.8% when $W = 1$ (Fig. 10) is used. The absence of strong sensitivity to $W$ is partly due to the normalization that we have described, and partly due to the fact that replacing $W = \sin\theta\exp(-(\Delta\phi)^2/2)$ by $W = 1$ does not alter the good phase agreement between measured and simulated CFs. It should also be noted that because both the tidal-fluctuation-induced coherence loss term $\exp(-(\Delta\phi)^2/2)$ and seafloor attenuation serve to preferentially attenuate steep-angle energy at higher frequencies, the optimal choice of the latter is expected to depend on whether or not the former is included

in $W$. Although replacing $W = 1$ by $W = \sin\theta\exp(-(\Delta\phi)^2/2)$ results in only slightly better agreement between simulated and measured CFs, that replacement represents an important, albeit incomplete, step toward describing the relevant underlying physics that contribute to the measured CF.

## V. SUMMARY

We have addressed the problem of waveform modeling of ambient noise CFs using measurements collected in a 100 m deep coastal ocean environment at both 5 and 10 km range. CFs are closely related, but not identical, to the GFs that describe propagation between the two measurement locations. To model CF waveforms, subtle differences between CFs and GFs must be accounted for. We have accounted for a phase difference that is predicted theoretically and we have introduced a physically motivated amplitude weighting function in our simulated CFs. The latter accounts for the directivity of the predominantly near-surface noise sources, and the effective filtering of high frequency and steep angle energy that results from coherently stacking many realizations of short-time estimates of the CF.

Measured CFs are, of course, also sensitive to the environment, so our focus on modeling CF waveforms has led us to simultaneously consider the inverse problem of estimating an optimal set of environmental parameters. This was accomplished using a simple parameterization of the environment, together with a brute-force search over a suitably bounded parameter space to identify the set of model parameters that minimize the chosen measure of misfit between measured and simulated CFs. That effort focused on analysis of CFs corresponding to an instrument separation of 5 km, both because those CFs have relatively high SNR and because the 5 km range environment is to a good approximation range independent. The CF corresponding to an instrument separation of 10 km was used as a consistency test of the environmental model parameters found using the 5 km data. The 10 km separation data were modeled using an adiabatic normal mode calculation, which showed fairly good agreement between measured and simulated CFs.

Our focus on modeling CF waveforms has led us to consider small but important differences between CFs and GFs, and to investigate the inverse problem. These issues are related inasmuch as one cannot expect to find good agreement between measured and simulated CFs unless the
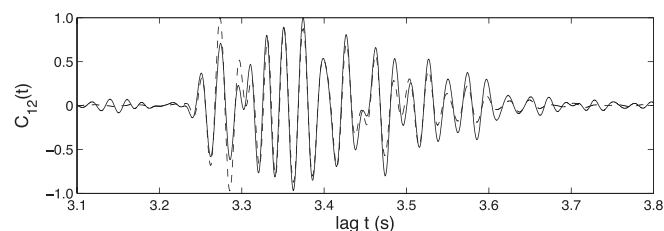


FIG. 10. Measured 1-2 instrument pair CF (solid curve) and corresponding simulated CF (dashed curve) computed using the optimal eight-parameter environmental model with $W = 1$.

environmental model used to produce the simulated CF is close to the true environment. Waveform matching of the type we have performed generally does not lead to a solution to the inverse problem that can be proved to be unique, even when active source transmissions are utilized. This problem is somewhat exacerbated in NI applications. That is because the optimal set of model parameters that one finds will, in general, depend on the weighting function $W(\omega, \theta)$ that is used to compute simulated CFs. A poor choice of $W(\omega, \theta)$ will lead to a biased set environmental model parameters. The form of $W(\omega, \theta)$ that we have chosen is a good approximation in the environment considered, but has clear limitations. The surface dipole excitation term $\sin \theta$ that we have used does not account for subsurface sound sources or scattering processes that lead to the conversion of steep angle energy to shallow angle energy. The Gaussian coherence loss term that we have used accounts only for tidal-fluctuation-induced coherence loss, and makes the idealized assumption that tidally induced sea surface height fluctuations have a Gaussian distribution. No other coherence loss mechanism was accounted for in our simulated CFs. In measured CFs, there is no simple way to distinguish between coherence loss mechanisms and attenuation mechanisms.

With the aforementioned limitations and caveats, we have computed simulated CFs that account for the theoretically predicted phase difference between CFs and GFs, and that include a physically motivated weighting function $W(\omega, \theta)$ that is a good approximation in the environment considered. Simulated CFs were used as the basis for a simple treatment of the inverse problem that resulted in an environmental model for which simulated CFs were shown to be in good agreement with their measured counterparts for instrument separations of both 5 and 10 km.

## APPENDIX

A simple derivation of the fundamental results of acoustic NI in a stationary environment is presented. The argument presented assumes weak dissipation, thereby avoiding a divergent correlation function and an indeterminant singular limit.

Convolutions and cross-correlations appear in the arguments that follow. Consider real-valued functions $f_1(t)$ and $f_2(t)$. Convolution of $f_1(t)$ and $f_2(t)$ is defined as $f_1(t) * f_2(t) = \int_{-\infty}^{\infty} d\tau f_1(\tau) f_2(t - \tau)$. The cross-correlation of $f_1(t)$ and $f_2(t)$ is defined as $f_1(t) * f_2(-t) = \int_{-\infty}^{\infty} d\tau f_1(\tau) f_2(t + \tau)$. Let $\bar{f}_1(\omega) = \int_{-\infty}^{\infty} f_1(t) e^{i\omega t} dt$ denote the Fourier transform of $f_1(t)$; all variables of interest are real-valued, so it is

assumed that $\bar{f}_1(-\omega) = \bar{f}_1^*(\omega)$, where the superscript "*" denotes complex conjugation. The Fourier transform of the convolution $f_1(t) * f_2(t)$ is $\bar{f}_1(\omega)\bar{f}_2(\omega)$, and the Fourier transform of the cross-correlation $f_1(t) * f_2(-t)$ is $\bar{f}_1(\omega)\bar{f}_2^*(\omega)$.

We formulate the acoustic NI problem in terms of the acoustic pressure $p$ because this is the quantity that is normally measured. Neglecting dissipation (for now), the time-dependent acoustic pressure $p(\mathbf{x}|\mathbf{x}_0, t)$ at position $\mathbf{x}$ due to a transient point source, at position $\mathbf{x}_0$ and with time history $s(t)$, satisfies

$$\left(\nabla^2 - \frac{1}{c^2(\mathbf{x})}\frac{\partial^2}{\partial t^2}\right) p(\mathbf{x}|\mathbf{x}_0, t) = -\delta(\mathbf{x} - \mathbf{x}_0)s(t).$$

Equivalently, $p(\mathbf{x}|\mathbf{x}_0, t) = s(t) * G(\mathbf{x}|\mathbf{x}_0, t)$ where the GF $G(\mathbf{x}|\mathbf{x}_0, t)$ satisfies

$$\left(\nabla^2 - \frac{1}{c^2(\mathbf{x})}\frac{\partial^2}{\partial t^2}\right) G(\mathbf{x}|\mathbf{x}_0, t) = -\delta(\mathbf{x} - \mathbf{x}_0)\delta(t),$$

or, in the frequency domain, $\bar{p}(\mathbf{x}|\mathbf{x}_0, \omega) = \bar{s}(\omega)\bar{G}(\mathbf{x}|\mathbf{x}_0, \omega)$ where $\bar{G}(\mathbf{x}|\mathbf{x}_0, \omega)$ satisfies

$$(\nabla^2 + k^2(\mathbf{x}))\bar{G}(\mathbf{x}|\mathbf{x}_0, \omega) = -\delta(\mathbf{x} - \mathbf{x}_0)$$

and $k^2(\mathbf{x}) = \omega^2/c^2(\mathbf{x})$. In an unbounded homogeneous environment $\bar{G}(\mathbf{x}|\mathbf{x}_0, \omega) = e^{ikr}/(4\pi r)$ and $G(\mathbf{x}|\mathbf{x}_0, t) = \delta(t - r/c)/(4\pi r)$ where $r = |\mathbf{x} - \mathbf{x}_0|$.

Assume a random distribution of discrete point sources at positions $\mathbf{x}_i$ and with time histories $s_i(t)$. Then $p(\mathbf{x}_A|\mathbf{x}_i, t) = s_i(t) * G(\mathbf{x}_A|\mathbf{x}_i, t)$ is the contribution to the acoustic pressure at location $\mathbf{x}_A$ from the source at $\mathbf{x}_i$. Similarly, the acoustic pressure at $\mathbf{x}_B$ due to the source at $\mathbf{x}_j$ is $p(\mathbf{x}_B|\mathbf{x}_j, t) = s_j(t) * G(\mathbf{x}_B|\mathbf{x}_j, t)$. Now sum up the contributions from all of the random sources and compute the cross-correlation of the acoustic pressures at locations $A$ and $B$:

$$\begin{aligned} C_{AB}(t) &= \sum_i p(\mathbf{x}_A|\mathbf{x}_i, t) * \sum_j p(\mathbf{x}_B|\mathbf{x}_j, -t) \\ &= \sum_i \sum_j s_i(t) * G(\mathbf{x}_A|\mathbf{x}_i, t) * s_j(-t) * G(\mathbf{x}_B|\mathbf{x}_j, -t) \\ &= D(t) * \sum_i G(\mathbf{x}_A|\mathbf{x}_i, t) * G(\mathbf{x}_B|\mathbf{x}_i, -t). \end{aligned}$$

We have assumed that the acoustic sources are independent and approximately $\delta$-correlated,

$$s_i(t) * s_j(-t) = \delta_{ij} D(t). \tag{A1}$$

Equivalently, $\bar{s}_i(\omega)\bar{s}_j^*(\omega) = \delta_{ij}\bar{D}(\omega)$. Note that $\bar{D}(\omega) = |\bar{s}_i|^2$ is real, or, equivalently, has zero phase. This condition is satisfied in all of the processing performed in this paper. The above argument can be modified to account for a continuum of sources. The result is

$$C_{AB}(t) = D(t) * \int\int\int d\mathbf{x}\, G(\mathbf{x}_A|\mathbf{x}, t) * G(\mathbf{x}_B|\mathbf{x}, -t). \tag{A2}$$

J. Acoust. Soc. Am. **138** (3), September 2015

Zang *et al.*    1331

[The dimensions of $D(t)$ are different in the discrete and continuum problems, but that subtlety has no bearing on the arguments that follow. We use only Eq. (A2) below.]

In the presence of weak dissipation, which is assumed to be proportional to $\omega$ times the parameter $\epsilon/2$, the GF $\bar{G}(\mathbf{x}|\mathbf{x}_A, \omega)$ at $\mathbf{x}$, corresponding to point source excitation at $\mathbf{x}_A$, satisfies

$$(\nabla^2 + k^2 + i\omega\epsilon/2)\bar{G}(\mathbf{x}|\mathbf{x}_A, \omega) = -\delta(\mathbf{x} - \mathbf{x}_A). \qquad (A3)$$

Similarly, $\bar{G}$ at point $\mathbf{x}$ excited by a point source at $\mathbf{x}_B$ satisfies

$$(\nabla^2 + k^2 + i\omega\epsilon/2)\bar{G}(\mathbf{x}_B|\mathbf{x}, \omega) = -\delta(\mathbf{x} - \mathbf{x}_B). \qquad (A4)$$

Due to reciprocity $\bar{G}(\mathbf{x}|\mathbf{x}_A, \omega)$ is equal to $\bar{G}(\mathbf{x}_A|\mathbf{x}, \omega)$, and $\bar{G}(\mathbf{x}|\mathbf{x}_B, \omega)$ is equal to $\bar{G}(\mathbf{x}_B|\mathbf{x}, \omega)$. Multiplication of Eq. (A3) by $\bar{G}^*(\mathbf{x}_B|\mathbf{x}, \omega)$, followed by integration over $\mathbf{x}$, and complex conjugation of left- and right-hand sides gives

$$\iiint d\mathbf{x}\, \bar{G}(\mathbf{x}_B|\mathbf{x}, \omega)(\nabla^2 + k^2 - i\omega\epsilon/2)\bar{G}^*$$
$$\times (\mathbf{x}_A|\mathbf{x}, \omega) = -\bar{G}(\mathbf{x}_B|\mathbf{x}_A, \omega). \qquad (A5)$$

Multiplication of Eq. (A4) by $\bar{G}^*(\mathbf{x}_A|\mathbf{x}, \omega)$, followed by integration over $\mathbf{x}$ gives

$$\iiint d\mathbf{x}\, \bar{G}^*(\mathbf{x}_A|\mathbf{x}, \omega)(\nabla^2 + k^2 + i\omega\epsilon/2)$$
$$\times \bar{G}(\mathbf{x}_B|\mathbf{x}, \omega) = -\bar{G}^*(\mathbf{x}_A|\mathbf{x}_B, \omega). \qquad (A6)$$

Subtracting Eq. (A6) from Eq. (A5) gives

$$Q - i\omega\epsilon \iiint d\mathbf{x}\bar{G}(\mathbf{x}_B|\mathbf{x}, \omega)\bar{G}^*(\mathbf{x}_A|\mathbf{x}, \omega)$$
$$= \bar{G}^*(\mathbf{x}_A|\mathbf{x}_B, \omega) - \bar{G}(\mathbf{x}_B|\mathbf{x}_A, \omega), \qquad (A7)$$

where

$$Q = \iiint d\mathbf{x}\bar{G}(\mathbf{x}_B|\mathbf{x}, \omega)\nabla^2\bar{G}^*(\mathbf{x}_A|\mathbf{x}, \omega)$$
$$- \iiint d\mathbf{x}\bar{G}^*(\mathbf{x}_A|\mathbf{x}, \omega)\nabla^2\bar{G}(\mathbf{x}_B|\mathbf{x}, \omega)$$
$$= \iint d\sigma[\bar{G}(\mathbf{x}_B|\mathbf{x}, \omega)\nabla\bar{G}^*(\mathbf{x}_A|\mathbf{x}, \omega)$$
$$- \bar{G}^*(\mathbf{x}_A|\mathbf{x}, \omega)\nabla\bar{G}(\mathbf{x}_B|\mathbf{x}, \omega)] \cdot \hat{n}.$$

By reciprocity $\bar{G}(\mathbf{x}_B|\mathbf{x}_A, \omega) = \bar{G}(\mathbf{x}_A|\mathbf{x}_B, \omega)$, so the right-hand side of Eq. (A7) can be written $-2\,\text{Im}\,\bar{G}(\mathbf{x}_B|\mathbf{x}_A, \omega)$. The second form of $Q$ given above follows from applying the divergence theorem to $\iiint d\mathbf{x} \nabla \cdot [\bar{G}(\mathbf{x}_B|\mathbf{x}, \omega)\nabla\bar{G}^*(\mathbf{x}_A|\mathbf{x}, \omega) - \bar{G}^*(\mathbf{x}_A|\mathbf{x}, \omega)\nabla\bar{G}(\mathbf{x}_B|\mathbf{x}, \omega)]$. The integral in the latter form of $Q$ is a surface integral over the boundary of the $\mathbf{x}$-domain and $\hat{n}$ is a unit outward normal. That integral vanishes under most conditions of interest. In an unbounded homogeneous environment, consider the domain enclosed within a large sphere of radius $R$ centered at the midpoint between $\mathbf{x}_A$ and $\mathbf{x}_B$. Owing to dissipation, for large $R$, $\bar{G}$ and $\nabla\bar{G} \cdot \hat{n}$ approach

zero faster than $R^{-1}$, so $Q$ approaches 0 in the large $R$ limit. Note also that in an $\mathbf{x}$-domain bounded by a combination of rigid walls (where $\nabla\bar{G} \cdot \hat{n} = 0$) and pressure release surfaces (where $\bar{G} = 0$), each term in $Q$ vanishes so $Q = 0$. Setting $Q = 0$ in Eq. (A7) gives

$$-i\omega\epsilon \iiint d\mathbf{x}\bar{G}(\mathbf{x}_B|\mathbf{x}, \omega)\bar{G}^*(\mathbf{x}_A|\mathbf{x}, \omega)$$
$$= \bar{G}^*(\mathbf{x}_A|\mathbf{x}_B, \omega) - \bar{G}(\mathbf{x}_B|\mathbf{x}_A, \omega). \qquad (A8)$$

Transforming to the time domain gives

$$\epsilon\frac{d}{dt}\iint d\mathbf{x}\, G(\mathbf{x}_B|\mathbf{x}, t) * G(\mathbf{x}_A|\mathbf{x}, -t)$$
$$= G(\mathbf{x}_B|\mathbf{x}_A, -t) - G(\mathbf{x}_B|\mathbf{x}_A, t), \qquad (A9)$$

where "$*$" (not a superscript) denotes convolution. Recall that the convolution of $G(\mathbf{x}_B|\mathbf{x}, t)$ and $G(\mathbf{x}_A|\mathbf{x}, -t)$ is equivalent to the cross-correlation of $G(\mathbf{x}_B|\mathbf{x}, t)$ and $G(\mathbf{x}_A|\mathbf{x}, t)$.

Finally, differentiating Eq. (A2) and making use of Eq. (A9) gives

$$\frac{d}{dt}[\epsilon C_{AB}(t)] = D(t) * [G(\mathbf{x}_B|\mathbf{x}_A, -t) - G(\mathbf{x}_B|\mathbf{x}_A, t)]. \qquad (A10)$$

Dissipation plays an important role in the arguments leading to Eq. (A10). The assumptions that we have made about the distribution and time history of the sources lead to a divergent $C_{AB}$ in the limit $\epsilon \to 0$; that limit is a singular limit. More generally, $C_{AB}(t)$ increases in magnitude with decreasing $\varepsilon$. For small $\varepsilon$, we may think of $\epsilon C_{AB}(t)$ as the effective correlation function and approximate this quantity as a constant times a long-time, but finite-time, approximation to the correlation function, and replace the GFs on the right-hand side of Eq. (A10) with their dissipationless counterparts.

[1]S. M. Rytov, Yu. A. Kravtsov, and V. I. Tatarskii, *Principles of Statistical Radiophysics. 3: Elements of Random Fields* (Springer, New York, 1989).
[2]O. I. Lobkis and R. L. Weaver, "On the emergence of the Green's function in the correlations of a diffuse field," J. Acoust. Soc. Am. **110**, 3011–3017 (2001).
[3]K. Wapenaar, "Retrieving the elastodynamic Green's function of an arbitrary inhomogeneous medium by cross correlation," Phys. Rev. Lett. **93**, 254301 (2004).
[4]R. Snieder, "Extracting the Green's function from the correlation of coda waves: A derivation based on stationary phase," Phys. Rev. E **69**, 046610 (2004).
[5]R. L. Weaver and O. I. Lobkis, "Fluctuations in diffuse field-field correlations and the emergence of the Green's function in open systems," J. Acoust. Soc. Am. **117**, 3432–3439 (2005).
[6]K. G. Sabra, P. Roux, and W. A. Kuperman, "Emergence rate of the time-domain Green's function from the ambient noise cross-correlation function," J. Acoust. Soc. Am. **118**, 3524–3531 (2005).
[7]O. A. Godin, "Recovering the acoustic Green's function from ambient noise cross-correlation in an inhomogeneous moving medium," Phys. Rev. Lett. **97**, 054301 (2006).
[8]O. A. Godin, "Retrieval of Green's functions of elastic waves from thermal fluctuations of fluid-solid systems," J. Acoust. Soc. Am. **125**, 1960–1970 (2009).
[9]J. Garnier and J. Papanicolaou, "Passive sensor imaging using cross correlations of noisy signals in a scattering medium," SIAM J. Imaging Sci. **2**, 396–437 (2009).

[10] R. B. Weaver, B. Froment, and M. Campillo, "On the correlation of non-isotropically distributed ballistic scalar diffuse waves," J. Acoust. Soc. Am. **126**, 1817–1826 (2009).

[11] O. A. Godin, "Cross-correlation function of acoustic fields generated by random high- frequency sources," J. Acoust. Soc. Am. **128**, 600–610 (2010).

[12] M. G. Brown, "Noise interferometry in an inhomogeneous environment in the geometric limit," J. Acoust. Soc. Am. **130**, EL173–EL179 (2011).

[13] N. A. Zabotin and O. A. Godin, "Emergence of acoustic Green's functions from time averages of ambient noise," Acta Acust. Acust. **97**, 44–53 (2011).

[14] M. Campillo and A. Paul, "Long-range correlations in the diffuse seismic coda," Science **299**, 547–549 (2003).

[15] N. M. Shapiro, M. Campillo, L. Stehly, and M. Ritzwoller, "High resolution surface wave tomography from ambient seismic noise," Science **307**, 1615–1618 (2005).

[16] Y. Yang, M. H. Ritzwoller, A. L. Levshin, and N. M. Shapiro, "Ambient noise Rayleigh wave tomography across Europe," Geophys. J. Int. **168**, 259–274 (2007).

[17] M. Campillo and P. Roux, "Seismic imaging and monitoring with ambient noise correlations," in *Treatise of Geophysics*, edited by B. Romanowicz and A. Dziewonski (Elsevier, Amsterdam, 2014), Vol. 1, pp. 256–271.

[18] T. L. Duvall, Jr., S. M. Jeffferies, J. W. Harvey, and M. A. Pomerantz, "Time-distance helioseismology," Nature **362**, 430–432 (1993).

[19] J. E. Rickett and J. F. Claerbout, "Calculation of the Sun's impulse response by multi-dimensional spectral factorization," Sol. Phys. **192**, 203–210 (2000).

[20] M. M. Haney, "Infrasonic ambient noise interferometry from correlations of microbaroms," Geophys. Res. Lett. **36**, L19808, doi:10.1029/2009GL040179 (2009).

[21] J. T. Fricke, L. G. Evers, P. S. M. Smets, K. Wapenaar, and D. G. Simons, "Infrasonic interferometry applied to microbaroms observed at the Large Aperture Infrasound Array in the Netherlands," J. Geophys. Res.: Atmos. **119**, 9654–9665 (2014).

[22] O. A. Godin, V. G. Irisov, and M. I. Charnotskii, "Passive acoustic measurements of wind velocity and sound speed in air," J. Acoust. Soc. Am. **135**(2), EL68–EL74 (2014).

[23] R. Snieder and E. Safak, "Extracting the building response using seismic interferometry; Theory and application to the Millikan Library in Pasadena, California," Bull. Seismol. Soc. Am. **96**, 586–598 (2006).

[24] K. G. Sabra, E. S. Winkel, D. A. Bourgoyne, B. R. Elbing, S. L. Ceccio, M. Perlin, and D. R. Dowling, "Using cross correlations of turbulent flow-induced ambient vibrations to estimate the structural impulse response. Application to structural health monitoring," J. Acoust. Soc. Am. **121**, 1987–2005 (2007).

[25] O. A. Godin, N. A. Zabotin, A. F. Sheehan, and J. A. Collins, "Interferometry of infragravity waves off New Zealand," J. Geophys. Res. Oceans **119**(2), 1103–1122 (2014).

[26] P. Roux, W. A. Kuperman and the NPAL Group, "Extracting coherent wave fronts from acoustic ambient noise in the ocean," J. Acoust. Soc. Am. **116**, 1995–2003 (2004).

[27] L. A. Brooks and P. Gerstoft, "Ocean acoustic interferometry," J. Acoust. Soc. Am. **121**, 3377–3385 (2007).

[28] S. E. Fried, W. A. Kuperman, K. G. Sabra, and P. Roux, "Extracting the local Green's function on a horizontal array from ambient ocean noise," J. Acoust. Soc. Am. **124**, EL183–EL188 (2008).

[29] L. A. Brooks and P. Gerstoft, "Green's function approximation from cross-correlations of 20–100 Hz noise during a tropical storm," J. Acoust. Soc. Am. **125**, 723–734 (2009).

[30] O. A. Godin, N. A. Zabotin, and V. V. Goncharov, "Ocean tomography with acoustic daylight," Geophys. Res. Lett. **37**, L13605, doi:10.1029/2010GL043623 (2010).

[31] O. A. Godin, "On the possibility of using acoustic reverberation for remote sensing of the ocean dynamics," Acoust. Phys. **58**(1), 129–138 (2012).

[32] K. G. Sabra, S. Fried, W. A. Kuperman, and M. Prior, "On the coherent components of low-frequency ambient noise in the Indian Ocean," J. Acoust. Soc. Am. **133**, EL20–EL25 (2013).

[33] S. E. Fried, S. C. Walker, W. S. Hodgkiss, and W. A. Kuperman, "Measuring the effect of ambient noise directionality and split-beam processing on the convergence of the cross-correlation function," J. Acoust. Soc. Am. **134**, 1824–1832 (2013).

[34] S. W. Lani, K. G. Sabra, W. S. Hodgkiss, W. A. Kuperman, and P. Roux, "Coherent processing of shipping noise for ocean monitoring," J. Acoust. Soc. Am. **133**, EL108–EL113 (2013).

[35] M. Siderius, C. H. Harrison, and M. B. Porter, "A passive fathometer technique for imaging seabed layering using ambient noise," J. Acoust. Soc. Am. **120**, 1315–1323 (2006).

[36] M. Siderius, H. Song, P. Gerstoft, W. S. Hodgkiss, P. Hursky, and C. Harrison, "Adaptive passive fathometer processing," J. Acoust. Soc. Am. **127**, 2193–2200 (2010).

[37] C. Yardim, P. Gerstoft, W. S. Hodgkiss, and J. Traer, "Compressive geoacoustic inversion using ambient noise," J. Acoust. Soc. Am. **135**, 1245–1255 (2014).

[38] O. A. Godin, "Accuracy of the deterministic travel times retrieval from cross-correlations of non-diffuse ambient noise," J. Acoust. Soc. Am. **126**, EL183–EL189 (2009).

[39] M. G. Brown, O. A. Godin, N. J. Williams, N. A. Zabotin, L. Zabotina, and G. J. Banker, "Acoustic Green's function extraction from ambient noise in a coastal ocean environment," Geophys. Res. Lett. **41**, 5555–5562, doi:10.1002/2014GL060926 (2014).

[40] O. A. Godin, M. G. Brown, N. A. Zabotin, L. Zabotina, and N. J. Williams, "Passive acoustic measurement of flow velocity in the Straits of Florida," Geosci. Lett. **1**, 16 (2014).

[41] J. A. Hildebrand, "Anthropogenic and natural sources of ambient noise in the ocean," Mar. Ecol. Prog. Ser. **395**, 5–20 (2009).

[42] D. S. Ahluwalia and J. B. Keller, "Exact and asymptotic representations of the sound field in a stratified ocean," in *Wave Propagation and Underwater Acoustics*, Lecture Notes in Physics, Vol. 70, edited by J. B. Keller and J. S. Papadakis (Springer, New York, 1977).

[43] L. M. Brekhovskikh and Yu. P. Lysanov, *Fundamentals of Ocean Acoustics*, 3rd ed. (Springer, New York, 2003).

[44] M. B. Porter, "The KRAKEN normal mode program," http://oalib.hlsresearch.com/Modes/kraken.pdf (Last viewed 3/19/2015).

[45] F. S. Anselmetti, G. A. von Salis, K. J. Cunningham, and G. P. Eberli, "Acoustic properties of Neogene carbonates and siliciclastics from the subsurface of the Florida Keys: Implications for seismic reflectivity," Mar. Geol. **144**, 9–31 (1997).

[46] F. B. Jensen, W. A. Kuperman, M. B. Porter, and H. Schmidt, *Computational Ocean Acoustics* (Springer, New York, 2000), Chap. 1, 5.

[47] Y. Jiang, N. R. Chapman, and H. A. Deferrari, "Geoacoustic inversion of broadband data by matched beam processing," J. Acoust. Soc. Am. **119**, 3707–3715 (2006).

[48] C. L. Monjo, H. Nguyen, and H. A. Deferrari, "Modulations of detectable pulse response time spread in shallow water resulting from a combination of sound-speed variability and bottom loss," J. Acoust. Soc. Am. **102**, 2083–2097 (1997).